



UNIVERSITY OF LEEDS

This is a repository copy of *Parallelizing and Balancing Coupled DSMC/PIC for Large-scale Particle Simulations*.

White Rose Research Online URL for this paper:

<https://eprints.whiterose.ac.uk/184746/>

Version: Accepted Version

Proceedings Paper:

Qiu, H, Xu, C, Li, D et al. (3 more authors) (2022) Parallelizing and Balancing Coupled DSMC/PIC for Large-scale Particle Simulations. In: 2022 IEEE International Parallel and Distributed Processing Symposium (IPDPS). 2022 IEEE International Parallel and Distributed Processing Symposium (IPDPS), 30 May - 03 Jun 2022, Lyon, France. IEEE , pp. 390-401. ISBN 978-1-6654-8107-6

<https://doi.org/10.1109/IPDPS53621.2022.00045>

© 2022 IEEE. Personal use of this material is permitted. Permission from IEEE must be obtained for all other uses, in any current or future media, including reprinting/republishing this material for advertising or promotional purposes, creating new collective works, for resale or redistribution to servers or lists, or reuse of any copyrighted component of this work in other works.

Reuse

Items deposited in White Rose Research Online are protected by copyright, with all rights reserved unless indicated otherwise. They may be downloaded and/or printed for private study, or other acts as permitted by national copyright laws. The publisher or other rights holders may allow further reproduction and re-use of the full text version. This is indicated by the licence information on the White Rose Research Online record for the item.

Takedown

If you consider content in White Rose Research Online to be in breach of UK law, please notify us by emailing eprints@whiterose.ac.uk including the URL of the record and the reason for the withdrawal request.



eprints@whiterose.ac.uk
<https://eprints.whiterose.ac.uk/>

Parallelizing and Balancing Large-scale Particle Simulations via Coupled DSMC/PIC

Abstract—Particle simulations are important workloads in high performance and parallel computing. Due to massive particle migration between parallel processes during simulations, efficient and balanced parallel computing is a practical challenge in large-scale realistic particle applications. This paper proposes a novel approach to enable highly-efficient dynamic load balance in a coupled DSMC/PIC solver for large-scale numerical simulations of the plasma plume. We employ dual unstructured grids of different granularity, with a coarse grid for DSMC simulations of flow fields and an embedded fine grid for PIC simulations of electric fields, to facilitate coupled DSMC/PIC calculation and grid partition for parallel computing. We then design and implement a centralized as well as a distributed communication strategies to dynamically migrate particles among arbitrary parallel processes. During the timestep iterations, we present a lightweight dynamic load balancer, composed of a load imbalance factor, a weighted load model and an efficient grid remapping mechanism, to adaptively rebalance the simulation among parallel processes with little extra overheads. We perform 3D unsteady simulations of the plasma plume induced by the pulsed vacuum arc in a cylindrical nozzle with hydrogen atoms and ions to validate the coupled solver. Parallel performance results scaling up to thousands of processes with billions of particles demonstrate the efficiency and effectiveness of our dynamic load balancer and parallel implementation.

Index Terms—Coupled DSMC/PIC, The plasma plume, Parallel computing, Dynamic load balance, Particle migration

I. INTRODUCTION

Particle simulation is widely used to model the physical world in many scientific and engineering subjects. It is a crucial application class on high-performance computing (HPC) systems. The plasma plume¹ is a typical particle simulation application and is key to enable research in fields like aerospace propulsion [1]–[3], industrial coatings [4], [5], and nuclear fusion reactors [6], [7].

The plasma plume induced by the pulsed vacuum arc has important applications in high-stability plasma devices. It usually flows in the millimeter range, incurring a series of complex thermochemical non-equilibrium reactions and wall interactions in the microsecond scale. Because of the high number of particles evaporated and the high particle density (e.g., $10^{18}/m^3$ to $10^{22}/m^3$), the corresponding plasma plume is very rarefied, and the resulting Knudsen number is greater than 0.1. Under such a setup, traditional Computational Fluid Dynamics (CFD) methods based on the Navier-Stokes equations are ill-suit for plasma plume simulation. As a result,

¹The *plasma plume* includes steam, plasma, molecular clusters, and surface debris. The steam and plasma are jetted back at ultra-high speeds of tens of kilometres per second.

the flow problem of plasma plume typically needs to be solved based on the Boltzmann equations [8].

The state-of-the-art approach for simulating plasma plumes combines Direct Simulation Monte Carlo (DSMC) [9] and Particle in Cell (PIC) [10], [11] methods. DSMC is proven to be effective in solving problems at the micro-level for rarefied gas flows, such as simulating the movement and collision between particles. Using the classical Bird’s algorithm [8], DSMC can achieve consistent results as the Boltzmann equations. PIC is useful for tracking a large volume of particles and their interactions. By coupling DSMC and PIC, one can model a large number of particles and their behavior at the micro-level. The combination allows the simulation system to effectively model complex physical phenomena in the plasma plume induced by a pulse vacuum arc.

Although coupled DSMC/PIC can achieve accurate particle simulation, this strategy requires more memory and computation resources than traditional CFD simulation techniques. One of the practical challenges in applying coupled DSMC/PIC to particle simulations in a distributed computing environment is to achieve dynamic load balance across simulation iterations. As we iterate the simulation timesteps, particles can move and may cross their grid cells. As such, the simulation algorithm must re-decompose the grid and then redistribute simulation particles between parallel processes after a certain number of timesteps. Without a proper load balancing strategy, the simulation workload can be unevenly distributed among parallel processes, where some are waiting for others to complete while others can be overloaded with too many particles. To improve the performance of large-scale particle simulations, we need to find ways to dynamically re-balance the simulation loads among parallel processes across timestep iterations.

This paper aims to provide a better approach for applying coupled DSMC/PIC to large-scale numerical particle simulations. To have a concrete application context, we choose plasma plume simulations as a case study but our approach can generalize to many other particle simulation workloads. Our approach offers several new optimizations for coupled DSMC/PIC simulations. These include a novel grid-based simulation scheme, a weighted load model to capture the importance of both particles and grid calculations, and the use of the Kuhn-Munkres (KM) algorithm [12], [13] to reduce the overhead of grid remapping.

Unlike prior work that employs two *structured* grids to implement the coupled DSMC/PIC algorithm [2], our approach exploits two *unstructured* grids to facilitate the coupled calculation and parallelization. Unstructured grids permit closer to

real-world simulation for many applications because particles can move in any manner, but care must be taken to identify neighboring elements. Unstructured grids are fundamentally different from structured ones, where particles are well ordered, and a simple indexing scheme can be used to label particles and identify neighbors.

Specifically, our unstructured-grided scheme incorporates a coarse and a fine tetrahedral grid. In the coarse tetrahedral grid, we constraint the cell size by the mean free path² of particles, and perform DSMC simulations of flow fields. In the fine tetrahedral grid, we constraint the cell size by the Debye length³, and perform PIC simulations of electric fields. The fine tetrahedral grid is entirely nested in the coarse grid (see Fig. 2 for an example). As a result, we only need to distribute the coarse grid across MPI processes where each MPI process can perform both DSMC and PIC simulations within different grids. Coupled DSMC/PIC along with the combination of two unstructured grids enable us to simulate a wider range of simulation setups involving complex phenomena and realistic geometries, compared to existing approaches [9]–[11].

Our work demonstrates the benefits of alternative implementations for a distributed, coupled DSMC/PIC solver. Unlike prior work that solely employs a distributed communication scheme, we offer both centralized and distributed communication schemes. We empirically demonstrate that the centralized communication strategy can outperform the distributed counterpart in certain simulation setups (e.g., with fewer simulated particles). A centralized scheme also incurs a low memory footprint, making it suitable for simulating large problems.

Armed with our grid strategy and communication schemes, we implement a lightweight dynamic load balancer to adaptively rebalance the simulation among MPI processes during the timestep iterations. As the particles can move across grid cells across iterations, leading to load imbalance among simulation grids, we adopt a weighted load model to guide dynamic mapping from grids to parallel MPI workers. We then employ the KM algorithm to reduce the overhead of work redistribution. We note that our work is the first to use the KM algorithm for dynamic work distribution in coupled DSMC/PIC. Our load balancer dynamically evaluates the load balance metric of work distribution across timesteps using the weighted model. It then redistributes the work across parallel processes if the quantified load imbalance is greater than a pre-defined threshold.

We evaluate our coupled solver by applying it to simulate unsteady plasma plume with particles of *hydrogen atoms* (H) and *ions* (H^+) induced by a pulsed vacuum arc in a 3D cylindrical nozzle. We test the performance of our approach on three HPC platforms, including two distinct Intel CPU-based clusters and an ARM CPU-based system. We showcase that our coupled DSMC/PIC solver delivers state-of-the-art plasma

²The *mean free path* is the average distance over which a moving particle (e.g., an atom, molecule, or photon) substantially changes its direction or energy, as a result of one or more successive collisions with other particles.

³In plasma, the *Debye length* is a measure of a charge carrier's net electrostatic effect in a solution and how far its electrostatic effect persists.

plume simulation performance, scaling well to thousands of processes with billions of particles.

This paper makes the following contributions:

- It is the first work to employ two unstructured grids for coupled DSMC/PIC simulations (Section IV);
- It presents a novel work scheduling scheme for particle simulations by employing a weighted load-balance model and the KM algorithm (Section V);
- It provides quantified analysis, showing the benefits and trade-offs of distributed and centralized communications in distributed particle simulations (Section VII-D).

II. RELATED WORK

Several studies have shown the efficiency of parallelizing coupled DSMC/PIC solvers. Aleph [14] is a coupled DSMC/PIC solver for simulating low-temperature plasma. It can simulate complex 3D models using unstructured tetrahedral grids. Based on Aleph, researchers have performed large-scale DSMC/PIC simulations with up to billions of simulation particles and thousands of cores [15], [16]. Other works [17] use the parallel-coupled PIC/DSMC algorithm to simulate the active plasma flow and chemical reactions in a rarefied condition. The work presented in [18] implemented a parallel high-order DSMC/PIC solver using MPI to simulate the 250ps diffusion process of a laser-driven plasma plume. The solver is based on 3D unstructured hexahedral grids, and the electromagnetic field is discretized using the Discontinuous Galerkin Method [19]. The SUGAR (Scalable Unstructured Gas dynamics with Adaptive mesh Refinement) software [20] uses MPI for parallel computing. SUGAR can simulate the ion thruster plume, including MEX (Momentum Exchange) collision and CEX (Charge Exchange) collision between neutral particles and charged particles. A GPU-based DSMC/PIC solver was presented in [21] using MPI+CUDA. This approach uses an octree to divide the computational domain and perform load balance according to particle numbers during simulations.

The aforementioned parallel implementations of coupled DSMC/PIC solvers mainly focus on the plasma plume generated by the electric thruster. Most of them only target the generation of plasma rather than the process of diffusion. Our work extends the coupled DSMC/PIC boundary to simulate the diffusion, collision, and reaction within a single framework. Due to dynamically changing simulation behaviour resulting from the complex simulation models, the parallelization method must be able to deal with the communications across arbitrary parallel processes. This challenge makes prior work infeasible to the simulation scenario we target. Our work addresses this challenge by implementing two communication strategies to migrate particles among arbitrary parallel processes. We then employ a dynamic load balancer to scale up the simulation performance to thousands of cores - which is the largest simulation setup seen to date for coupled DSMC/PIC. The scalability offered by our approach represents a significant improvement over the hundreds of cores scalability offered by existing coupled DSMC/PIC. On top of these, we also share our detailed sensitivity analysis on our design choices,

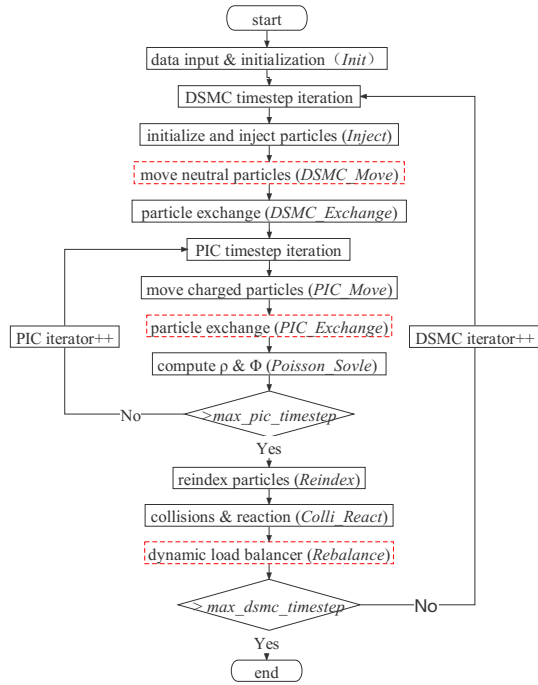


Fig. 1. The workflow of our coupled DSMC/PIC solver. The dotted rectangles highlight the new contributions introduced in this paper.

which we hope will be useful for further studies in parallel DSMC/PIC solutions.

III. IMPLEMENTATION OF THE COUPLED SOLVER

A. Infrastructures

Our work builds upon an in-house DSMC solver developed based on the seminar algorithm presented in [8]. This DSMC solver implemented various models to simulate the processes of collisions, wall interactions and chemical reactions of particles in the flow fields. After the DSMC solver have been used and validated for several years, a PIC solver is introduced to simulate the movement of charged particles according to the effects of electric fields. The two components form the coupled DSMC/PIC solver used in this work. Prior works [22], [23] have provided compelling evidence, showing the effectiveness and correctness of this coupled solver.

B. Simulation Workflow

Fig. 1 give the overall workflow of our coupled solver. The input to the solver is two unstructured grids and simulation parameters. These are passed into the initialization component (*Init*) to instantiate some internal data structures. The solver then iteratively goes through the DSMC and PIC simulation steps, detailed as follows.

DSMC timesteps. During a DSMC timestep, the *Inject* component initializes and injects simulation particles into the inlet randomly. The injection should ensure the velocity is perpendicular to the inlet and satisfies the physical law (i.e., the Maxwell distribution in our case). Next, the *DSMC_Move* component starts simulating the movement of neutral particles. In each DSMC timestep, neutral particles will move straightly

at a constant speed and can cross different grid cells or even move out of the computational domain.

PIC timesteps. A DSMC timestep typically contains multiple PIC timesteps, and the size of DSMC or PIC timesteps depends on the mean free path of particles [24]. In each PIC timestep, the *PIC_Move* component simulates the movement of the charged particles in the electric field. At the current timestep, the charged particles are driven by the electric field of the previous timestep. A key task of a PIC timestep is to determine the charged particle's velocity and position using the *Poisson_Solve* component. We elaborate on the *Poisson_Solve* component in Section III-C.

Particle numbering. The particle locations are likely to change during iterations. The location change can cause the change of particle distributions, which requires the simulator to renumber all particles in a uniform way to ensure each of them has a unique index number. This is performed by the *Reindex* component, which will also remove particles that moved out of the computational domain after a DSMC iteration.

Collision and reaction. Unlike prior work that mainly focuses on the generation of plasma, our DSMC solver also implements various collision and chemical reaction models [23] in the *Colli_React* component. In this paper, we adopt Bird's no time counter (NTC) method [?] to select collision pairs. After selecting the collision pairs, we determine whether the two particles will have a chemical reaction according to the particle types and the energy of the collision. We then perform chemical reactions for those particles.

Our extensions. The main contributions of this paper are highlighted using dotted rectangles in Fig. 1. Specifically, the *PIC_Exchange* and *DSMC_Exchange* components are responsible for two parallel communication strategies at the PIC and DSMC iterations, respectively. The communication strategies are described in Section IV-B. The *Rebalance* component is our dynamic load balancer, described in Section V.

C. Determining the Particle Velocity and Position with PIC

The velocity, v , and position, r , of particles can be acquired by solving the following kinetic equation [23] for plasma physics during a PIC timestep, t :

$$\begin{cases} \frac{dr}{dt} = v \\ m \frac{dv}{dt} = q(E + v \times B) \end{cases} \quad (1)$$

where m is the mass of the particles (given by the user), q is the charge for particles, B is the magnetic density and E is the electric field intensity. In this paper, we only consider the electrostatic field by assuming that there is no magnetic field (i.e., $B = 0$) or a constant magnetic field (i.e., B is a constant number given by the user). The solution of the kinetic equation determines the distribution function of the dynamical states of each individual particle.

We determine the relevant parameters of the kinetic equation as follows.

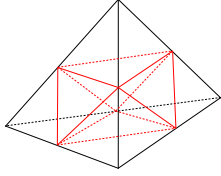


Fig. 2. A coarse tetrahedral grid cell for DSMC contains 8 fine tetrahedral grid cells for PIC.

Determine v and q . We use the Boris method [25] to calculate the numerical value of the velocity v . We then compute the charge density q , by interpolating the particle charge to the grid nodes, following the movement of charged particles.

Determine E . We compute E by solving Poisson’s equation for electrostatics:

$$\nabla \cdot E = \frac{\rho}{\epsilon_0} \quad (2)$$

where ρ is a total volume charge density, ϵ_0 is the permittivity⁴ of the medium, and ∇ is the Laplace operator. Here, the electric field intensity E , can be expressed as a negative gradient of the electric potential ϕ :

$$E = -\nabla\phi, \quad (3)$$

With (3), we convert Poisson’s equation in (2) to the following formula, by substituting E with $-\nabla\phi$:

$$\nabla \cdot E = \nabla \cdot (-\nabla\phi) = -\nabla^2\phi = \frac{\rho}{\epsilon_0} \quad (4)$$

We then solve (4) by discretizing it using the finite volume method [26] on unstructured grids to construct the following linear system:

$$K\phi = b \quad (5)$$

where K is the diagonally-dominant stiffness matrix constructed according to the grid topology, b is derived from boundary conditions and the electric potential. We use the linear system to derive ϕ , which is then used to compute E through (3). This process is performed by the *Poisson_Solve* component in Fig. 1. We note that solving (5) is a time-consuming process, and hence can benefit from parallel computing. In Section IV-C, we describe our parallelization strategy for solving the linear system.

IV. PARALLEL SOLVER IMPLEMENTATION

A. Grid Generation and Decomposition

Our coupled solver is designed and optimized for unstructured grids, focusing on tetrahedral grids in this paper. Under such a setting, each particle belongs to a grid cell, and the cell size is constrained by different particles. When applying DSMC to neutral particles, the cell size must satisfy two constraints. It should meet the mean free path limit of the particles and comply with the Debye length when applying PIC to charged particles for solving the electric potential (see

Section III-C). To meet the above constraints, our coupled DSMC/PIC solver first generates a coarse tetrahedral grid for DSMC. It then divides each coarse-grained grid cell into 8 smaller grid cells to form a fine grid for PIC. As shown in Fig. 2, this is realized by having each edge of the tetrahedron. The fine grid is embedded in the coarse grid to facilitate the coupled computation and grid decomposition for parallel computing. Since each fine-grained cell belongs to a coarse-grained cell, we only need to decompose the coarse grid for parallel computing. We then determine the mapping of fine-grained cells to parallel processes accordingly.

We utilize the graph partition method (*METIS_PartGraphKway*) from the METIS graph and mesh partitioning library [27] to decompose the grid. The end-user can supply a weight array to represent loads of grid cells and achieve specific load balance requirements for their applications. For the first decomposition, we do not provide the weight array to METIS. For the re-decomposition operations in our dynamic load balancer, we derive a load model from calculating a weight for each cell (see also Section V). After grid decomposition, each parallel process can perform simulation independently on its grid cells (and the associated particles).

B. Parallel Communication Strategies

For both PIC and DSMC simulations, the particles may move from one grid cell to another. The source and destination cells have been assigned to different parallel processes running on distributed machines. Since the migration distances of particles in our coupled algorithm can be long, the destination cell of a moving particle may belong to a domain that is far from the original domain. For this reason, the solver must be able to optimize the communications between arbitrary parallel processes. Unfortunately, the ghost cell immersed boundary method, which is often used in traditional CFD [28], is not feasible for our problem because it can only deal with the communication between the neighboring parallel processes. To this end, we propose two communication strategies to optimize particle migration among arbitrary processes. The two strategies are both implemented in *DSMC_Exchange* and *PIC_Exchange* components in Fig. 1.

1) *The centralized communication strategy:* Fig. 3 gives a simple illustration of the centralized communication strategy. Here, a centralized process (e.g., rank 0 in Fig. 3) is selected to manage the whole procedure of particle migration. The procedure consists of three stages: *gather*, *classify* and *scatter*. Each process sends the particles that will move to another process to the centralized process during the gathering stage. After gathering all migrating particles, the centralized process will classify them according to their destination processes. The particles, which may come from different source processes but move to the same destination, will be packed together. Finally, the centralized process scatters the packed particles to the corresponding processes.

2) *The distributed communication strategy:* As illustrated in Fig. 4, with a distributed communication strategy, each

⁴The permittivity is a measure of the electric polarizability of a dielectric.

Algorithm 1 The rebalance algorithm

Input: *cellnum*, *procsnum*, *T*, *Threshold*, *OriginalMapping*
Output: *FinalMapping*
1: compute *lii* according to (6)
2: *iterator* \leftarrow *iterator* + 1
3: **if** *iterator* < *T* \parallel *lii* < *Threshold* **then**
4: **return**
5: **end if**
6: **for** *i* = 0 \rightarrow *cellnum* **do**
7: compute *wl_i* according to (7)
8: *wl* \leftarrow *wl_i*
9: **end for**
10: *NewPartition* \leftarrow *METIS_PartGraphKway*(*cellnum*, *procsnum*, *wl*)
11: *FinalMapping* \leftarrow *Kuhn_Munkras*(*OriginMapping*, *NewPartition*)
12: **return** *FinalMapping*

In light of the above observation, we design and implement a dynamic load balancer in the coupled solver. Algorithm 1 outlines the working mechanism of the dynamic load balancer. Our load balance algorithm quantifies the load imbalance using an analytical model (Section V-A). It then uses a weighted load model to decompose the grids across parallel workers (Section V-B). During runtime, the load balancer periodically checks the imbalance indicator (*lii*) for a user-specified number of timestep iterations (i.e., *T*). If a *Threshold* is reached, it then re-decomposes the grid according to the load model and remaps the newly partitioned grid to parallel processes. The algorithm was implemented in the *Rebalance* component in the DSMC iterations as shown in Fig. 1.

A. The Load Imbalance Indicator

Our load imbalance indicator (*lii*) measures the execution time of different parallel processes and compares the maximum and minimum values. Our load imbalance indicator is formulated as:

$$lii = \frac{Time_{max_total} - Time_{max_pm} - Time_{max_poi}}{Time_{min_total} - Time_{min_pm} - Time_{min_poi}} \quad (6)$$

where the subscript “*max*” and “*min*” denote the corresponding processes with the measured maximum and minimum execution times respectively. $Time_{max_total} / Time_{min_total}$ is the total execution time, $Time_{max_pm} / Time_{min_pm}$ and $Time_{max_poi} / Time_{min_poi}$ are the time cost of particle migration and solving the Poisson’s equation respectively. Note that the time spending on particle migration (*DSMC_Exchange* and *PIC_Exchange*) and solving Poisson’s equation (*Poisson_Solve*) are largely constant.

We use *lii* to evaluate the load imbalance for a configurable number of DSMC iterations *T* (defined by the user). We set a load imbalance *Threshold*, and check if *lii* is larger than the *Threshold* for *T* DSMC iterations. If $lii > Threshold$ holds, we will perform the dynamic load balance optimization. *T* and *Threshold* can be selected according to specific simulation setups runs using an auto-tuning technique [31].

B. The Weighted Load Model

To initialize the simulation, we use METIS to decompose the grid for parallel computing solely according to the number of grid cells. Our dynamic load balancer may decide to re-decompose the grid during runtime to balance the number

of particles simulated by MPI processes. Our optimization strategy also needs to consider the requirement of the coupled computation: DSMC only simulates the neutral particles, and PIC only deals with the charged particle, and a DSMC timestep may contain multiple PIC timesteps. Because of these constraints, we should give different weights to neutral and charged particles when estimating the work for grid decomposition. For example, if each DSMC timestep contains 2 PIC timesteps, then the weight ratio *R* of charged particles and neutral particles should be 2 because there are twice more charged particles to be simulated than the natural particles within a DSMC step. Besides particles, some computations (e.g., *Colli_React* and *Poisson_Solve* in Fig. 1) are performed on grid cells, and each grid cell should also have its weight. Our design takes these constraints into consideration.

Specifically, our weighted load model (*wlm*) for the i^{th} grid cell wlm_i is defined as follows:

$$wlm_i = N_i + RC_i + W_{cell} \quad (7)$$

where N_i and C_i represents the number of neutral particles and charged particles in the grid cell respectively and W_{cell} represents the weight of the grid cell, taking the weight of a neutral particle as the baseline.

With (7) in place, we can calculate the combined weight for each grid cell and then provide the weight to the *METIS_PartGraphKway* graph partition tool in *METIS* to re-decompose the grid for parallel computing in the subsequent timesteps.

C. Efficient Grid Remapping

After grid re-decomposition, we need to redistribute the grid cells to parallel processes for subsequent simulations. This is also involved migrating particles within a process, or from grid cells to other processes. A naïve approach by randomly remapping grid cells can incur significant overhead and reduce the efficacy of our dynamic load balancer. For the example shown in Fig. 6, the mapping given in Fig. 6(c) is better than the one in Fig. 6(b). Fig. 6(c) requires moving just particles in cell 3, while Fig. 6(b) requires moving all particles in every cell across MPI ranks - e.g., cells 2 and 4 are moved from rank 0 in Fig. 6(a) to rank 2 in Fig. 6(b) and similarly for other cells. Due to the extensive work redistribution across computing nodes, Fig. 6(b) will lead to a higher communication overhead than Fig. 6(c).

This observation suggests that a good remapping strategy should try to remap the re-decomposed cells according to the original mapping. It should also minimize the total number of particles to be migrated during re-decomposition. Therefore, our remapping scheme aims to achieve these goals. To solve the remapping problem, we convert the grid remapping problem into the maximum weight matching problem in a bipartite graph. We then use the classical KM algorithm to solve the maximum weight matching problem. For the example shown in Fig. 6, our KM-based approach gives the optimal solution shown in Fig. 6(c).

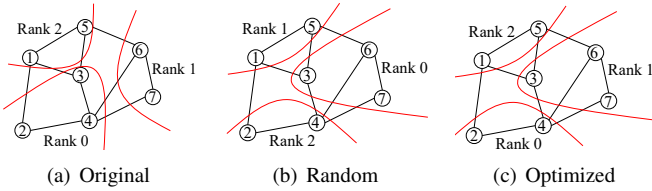


Fig. 6. An example of different grid mapping strategies. Fig. 6(a) is the original grid decomposition and mapping where the circle represents a grid cell. Fig. 6(b) is a possible random grid remapping after re-decomposition. Fig. 6(c) is an optimized remapping given by our approach.

VI. EXPERIMENTAL SETUP

A. Hardware Platforms

We evaluate our approach on three HPC systems. These include two x86 HPC clusters from the Tianhe-2 supercomputer [32] and the Beijing Beilong Super Cloud Computing (BSCC) infrastructure, and an ARMv8 based system from the Tianhe-3 exascale prototype supercomputer [33]. We run our solver on the CPU host solely as our implementation currently does not support accelerators.

The Tianhe-2 supercomputer. This is our main evaluation platform. Each Tianhe-2 compute node has two 12-core Intel Xeon E5-2692 v2 processors at 2.2GHz and 64GB of RAM. Compute nodes are connected through an in-house developed high-speed interconnection network, with a point-to-point bandwidth of 160 Gbps. Tianhe-2 implements a fat-tree communication topology and runs the Kylin OS with Linux kernel v2.6.32.

The BSCC supercomputer. Each BSCC compute node contains two 48-core Intel Xeon Platinum 9242 CPUs at 2.3 GHz and 384 GB of RAM. Compute nodes are connected via the InfiniBand, with a point-to-point bandwidth of 100 Gbps. This system runs CentOS with Linux kernel v3.10.0.

The ARM-based Tianhe-3 prototype. Each compute node of the Tianhe-3 prototype has a 64-core ARMv8-based Phytium 2000+ CPU at 2.2 GHz and 64GB of RAM. Compute nodes are connected through an in-house developed high-speed interconnection network, with a point-to-point bandwidth of 200 Gbps. This system implements a fat-tree communication topology and runs the Kylin OS with Linux kernel v4.4.0.

B. Software Implementations

Our coupled DSMC/PIC solver was implemented in C and compiled with GCC v11.2 with the “-O3” compiler option. We use MPICH v3.2 for parallel MPI communication, the KSP solver from PETSc v3.15.0 to solve Poisson’s equation and METIS v5.1.0 for domain decomposition.

C. Simulation Setup

In this paper, we simulate the diffusion, collision and reaction of the plasma plume induced by the pulsed vacuum arc in a 3D cylindrical nozzle. Fig. 7 depicts the simulation setup of the nozzle. We use the SALOME numerical simulation platform [34] to generate the tetrahedral grids for the cylindrical nozzle.

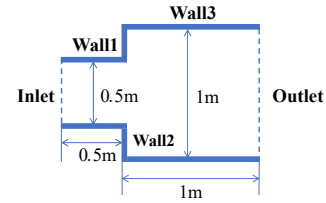


Fig. 7. The configuration of the cylindrical nozzle used in simulations.

TABLE I
THE PIC GRID CELL NUMBERS AND SCALING FACTORS OF DIFFERENT DATASETS USED IN VALIDATION AND PERFORMANCE TESTS.

	#PIC Cells	Scaling Factor (H)	Scaling Factor (H^+)
<i>Dataset 1</i>	55,576	1×10^{12}	6,000
<i>Dataset 2</i>	583,386	9.94×10^{10}	0.477
<i>Dataset 3</i>	583,386	9.94×10^{11}	4.77
<i>Dataset 4</i>	583,386	1.988×10^{11}	0.954
<i>Dataset 5</i>	2,242,948	1.4×10^{11}	12,500
<i>Dataset 6</i>	2,242,948	2.8×10^{11}	25,000

As listed in Table I, we used six datasets in our evaluation. We use *Dataset 1* to validate our implementation and the other five different datasets for performance tests. The solver converts the number density⁵ of realistic particles to the corresponding density of simulation particles using a scaling factor given in Table I. The scaling factor indicates the number of real particles to be represented by a simulation particle. By changing the scaling factors, we can easily vary the number of simulation particles and the corresponding computing load for the same number density of realistic particles. Once the grid is determined, we can then work out the timesteps of DSMC and PIC as well as the number density of particles accordingly.

In this work, we are mainly concerned about the dissociation of H and the recombination of H^+ . We set the particle velocity to $10000m/s$ and the wall temperature to $300K$. As the setting of particle density and the timestep size depend on the cell size, we will provide this information when discussing the relevant experiments. We run each simulation for 100 DSMC timesteps, where each DSMC timestep contains 2 PIC timesteps. We run each simulation setup 5 times and report the mean execution time across runs. We note that our evaluation setups represent real-life simulation setups.

VII. EXPERIMENTAL RESULTS

A. Validation of the Parallel Implementation

Setup. We use *Dataset 1* in Table I to validate our parallel implementation of the coupled DSMC/PIC solver. We set the number density of H to 7×10^{18} and the density of H^+ to 3×10^8 . The timestep sizes of DSMC and PIC are 2×10^{-7} and 1×10^{-7} respectively. The total simulation time is $20\mu s$.

Results. Fig. 8 shows the number density contours of H after 200 PIC timesteps of simulations from our parallel version

⁵The number density quantifies the degree of concentration of countable objects (particles, molecules, phonons, etc.) in physical space.

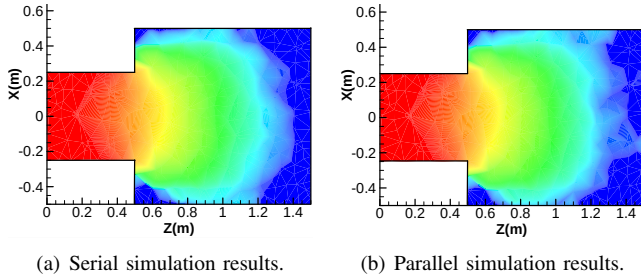


Fig. 8. The number density contours of H after 200 PIC timesteps of simulations from a serial version of the solver (a) and our parallel version of the solver (b).

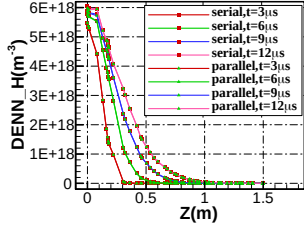


Fig. 9. The number density of H at selected points on the central axis given by the serial solver and our parallel solver.

and a serial version of the solver which was validated in prior work [23]. We observe some minor differences in the contours, and this is mainly due to random seed numbers used for simulations. To have a close examination, we further measured the number density of H at several points on the central axis of the cylinder. Fig. 9 shows the number density of H on the central axis given by the serial and the parallel solver when time t is $3\mu s$, $6\mu s$, $9\mu s$ and $12\mu s$. As can be seen from this diagram, curves at the same time point coincide, indicating consistency of parallel and serial runs.

B. Performance Results

Setup. We use *Dataset 2* in Table I to evaluate the strong scalability of the proposed approach on the Tianhe-2 supercomputer. According to the physical constraints of DSMC and PIC models, we set the number density of H and H^+ to 9.94×10^{19} and 4.77×10^7 respectively. In this dataset, the scaling factor of the DSMC and PIC is 9.94×10^{10} and 0.477 respectively, which means we need to deal with 10^9 simulation particles of H for DSMC, and 10^8 simulation particles of H^+ for PIC. The timestep of DSMC and PIC is set to 1.2586×10^{-6} and 6.293×10^{-7} respectively. For the parameters of the dynamic load balancer, we set *Threshold* to 2.0, *R* to 2, *T* to 20 and *W_{cell}* to 1. These parameters were automatically chosen during our pilot study on a different dataset using a sampling script. The effects of different parameters on the overall performance will be analyzed in Section VII-D. We take the results obtained using 24 processor cores as the baseline to measure the strong scalability. We then vary the number of processors using a maximum of 1563 cores on Tianhe-2.

Results. Fig. 10 and Table II summarize the results for distributed (DC) and centralized (CC) communication strategies

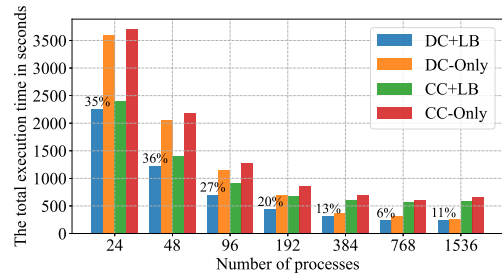


Fig. 10. The total execution time of different implementations scaling up to 1536 processes. The percentages on the bar indicate the performance enhancement when dynamic load balance is enabled

TABLE II
THE TOTAL EXECUTION TIME IN SECONDS IN STRONG SCALABILITY TESTS. DC AND CC DENOTE THE DISTRIBUTED AND THE CENTRALIZED COMMUNICATION STRATEGIES RESPECTIVELY. LB DENOTES THE ENABLING OF DYNAMIC LOAD BALANCE.

	Number of Processes						
	24	48	96	192	384	768	1536
DC+LB	2258	1230	706.4	445.2	317.4	240.1	245.8
DC-Only	3602	2058	1156	689.1	378.4	311.5	257.1
CC+LB	2396	1400	919.6	678.8	605.1	571.8	591.4
CC-Only	3702	2192	1274	855.4	698.2	610.7	665.4

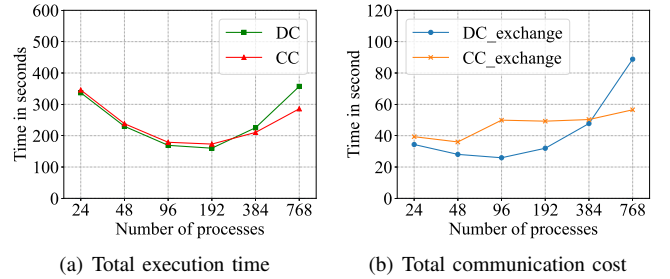


Fig. 11. Performance comparison of the two communication strategies on the BSCC supercomputer. DC/CC denote the total execution time of the two strategies. DC_exchange/CC_exchange denote the total communication costs using the distributed and the centralized strategy respectively.

when they are used together with and without dynamic load balance (+LB). As can be seen from Fig. 10, all four implementations give improved performance when scaling from 24 cores to 1536 cores. A maximum speedup of about 14x (DC-only) is achieved, indicating a scaling efficiency of about 22%. On Tianhe-2, the distributed communication strategy always outperforms the centralized communication strategy under different numbers of parallel processes, regardless of whether the dynamic load balancer is enabled or not. When the number of processes increases, the advantage of the distributed communication strategy is even larger. For example, the performance is improved by more than 60% when using the distributed strategy for 1536 cores.

C. Further Analysis of Scalability Evaluation

1) *Impact of load balancer:* For the distributed and centralized communication strategies, we observe significantly

TABLE III

THE TOTAL EXECUTION TIME IN SECONDS FOR PARTICLE MIGRATION

	Number of Processes						
	24	48	96	192	384	1536	
DC+LB	358.6	208.3	101.8	53.08	29.90	17.95	12.05
DC-Only	1106	769.2	408.2	201.5	130.8	69.69	35.17
CC+LB	359.1	192.7	113.4	59.59	41.64	26.96	22.16
CC-Only	1119	777.8	408.5	200.1	128.8	69.92	35.37

improved performance and a better scaling efficiency when our dynamic load balancer is enabled. Our load balancer is particularly useful when a small number of processes is used. For example, our load balancer improves the performance by about 40% and 36% for the distributed and the centralized strategies, respectively, when using 48 cores. As discussed in Section V, load imbalance in our test case is more severe when a smaller number of processes are used in the parallel simulation. In such settings, our dynamic load balancing strategy helps rebalance the simulation load, leading to better overall performance and scalability.

Since load imbalance mainly affects the performance of *DSMC_Move* and *PIC_Move*, we further analyze the effects of dynamic load balance on the two procedures in Table III. We can see that the execution time of *DSMC_Move* and *PIC_Move* is reduced to less than one-third of the original implementation without dynamic load balance, which further demonstrates the effectiveness of our rebalancing implementation.

2) *Distributed vs centralized communications*: While the distributed communication strategy gives better performance over the centralized counterpart on Tianhe-2, the centralized strategy could still be beneficial when the number of simulation particles is small, and the process number is large, as we have discussed in Section IV. A centralized scheme also incurs a low memory footprint, making it suitable for simulating large problems. To validate our hypothesis, we perform a further evaluation on the BSCC supercomputer using *Dataset 3* in Table I. In this dataset, we increase the scaling factors of DSMC and PIC to 9.94×10^{11} and 4.77, respectively. As a result, the numbers of simulation particles are reduced to 10^8 and 10^7 correspondingly. Fig. 11 shows the communication costs as well as the total execution time for the two strategies on the BSCC supercomputer with load balance enabled.

As shown in Fig. 11, for a smaller number of processes (e.g., less than 384), the total execution times of the two strategies are quite close, although the communication costs of the centralized strategy are larger than the distributed strategy. For 768 processes, the communication cost of the distributed strategy dramatically increased to as large as more than twice of the centralized strategy, which makes the whole solver using the distributed strategy slower than using the centralized strategy by about 25%. The comparison provides some interesting insights when choosing parallel communication modes of DSMC/PIC on different HPC platforms for different simulation configurations (e.g., simulation particles, the number of processes). Another disadvantage of the distributed

TABLE IV

BREAKDOWN OF THE TOTAL EXECUTION TIME IN SECONDS FOR MAIN PROCEDURES ON TIANHE-2 USING DC WITH LOAD BALANCE ENABLED.

	Number of Processes						
	24	48	96	192	384	768	1536
<i>DSMC_Move</i>	283	163	82.4	42.4	21.6	11.8	6.59
<i>DSMC_Exchange</i>	29.8	17.0	11.1	8.32	4.52	2.52	3.34
<i>Inject</i>	1622	812	420	210	104	52.4	31.0
<i>PIC_Move</i>	74.8	45.0	19.3	10.6	8.22	6.15	5.46
<i>PIC_Exchange</i>	68.0	44.5	31.7	25.1	20.5	20.1	28.8
<i>Poisson_Solve</i>	95.0	94.1	99.0	108	114	116	126
<i>Reindex</i>	13.9	6.00	2.50	1.29	0.77	0.37	0.19

communication strategy is that it demands more memory.

3) *Scalability bottleneck*: To find out the scalability bottleneck, we further examine the breakdown of the total execution time on Tianhe-2. Some most time-consuming procedures are listed in Table IV for the DC+LB implementation. Most procedures except *Poisson_Solve* show good strong scalability. For example, the parallel efficiency of *DSMC_Move*, *Inject* and *Reindex* remain above 67% when scaling to 1536 cores. The running time of particle migration is also not dominant. *Poisson_Solve* shows an extraordinary poor scalability to only 24 or 48 processes in our tests, making it a main bottleneck for the parallel performance of the coupled solver. One possible explanation for the poor scalability of *Poisson_Solve* is that the total number of grid cells of the nozzle (i.e., 583386) is not large enough for large-scale parallel solution of the Poisson's equation. In addition, the matrix K in Poisson's equation is a sparse matrix, and thus the ratio of communication to calculation is very high. Enlarging the grid cell number may improve the parallel scalability of *Poisson_Solve*. Meanwhile, the numbers of simulation particles also have a great impact on parallel scalability. More simulation particles indicate a decreasing communication-to-calculation ratio. In Fig. 10, we scale to 1536 cores with more simulation particles, and in Fig. 11 we only achieve scalability with no more than 192 cores for fewer simulation particles.

D. Sensitivity Tests

This section evaluates the robustness of our approach under different tuning parameters and MPI rank placements. We also test our approach on an additional ARM-based cluster, showing that our approach delivers portable performance across computing architectures.

1) *Dynamic load balancing*: We perform sensitivity tests on the Tianhe-2 supercomputer to further evaluate the impacts of different parameters in our dynamic load balance. This experiment was conducted on *Dataset 2* in Table I, but we observe similar results on other datasets.

Table V quantifies the importance of the KM algorithm. For our test scenarios, the KM algorithm plays an important role in *Rebalance* in reducing the overhead to about half of the original implementation without KM. When the process number is greater than 768, the effects of the KM algorithm

TABLE V
THE OVERHEAD IN SECONDS OF DYNAMIC LOAD BALANCE WITH/WITHOUT KM

	Number of Processes						
	24	48	96	192	384	768	1536
DC with KM	9.61	5.42	3.38	1.84	1.08	0.64	0.51
DC without KM	11.5	5.82	3.50	2.01	1.24	0.79	0.63
CC with KM	64.3	63.5	65.1	20.5	8.81	13.0	0.09
CC without KM	121	122	75.4	49.5	35.1	13.3	0.09

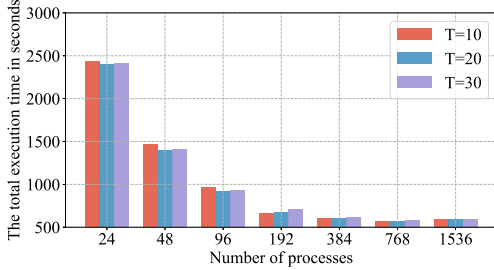


Fig. 12. Effects of T for the DC strategy on Tianhe-2.

is not obvious. This is because the number of the rebalancing operations decreases as the process number increases. For the 1536-process run, we only perform one dynamic load balance when simulating 200 PIC timesteps. This can also explain why the load balancing overhead declines as the process number increases.

Fig. 12 shows the effects of T . Typically when T is small, the solver will perform more rebalancing operations, and the overhead may possibly exceed the rebalancing benefit; when T is large, the load imbalance will become severe and degrade the overall performance. As we can see from Fig. 12, $T = 20$ is slightly better than $T = 10$ and $T = 30$ when using no more than 96 processes. With the process number increases, $T = 10$ is slightly better than $T = 20$ and $T = 30$.

Table VI shows the effects of various W_{cell} in (7). Since we find that a small change of W_{cell} has little effect in the tests, W_{cell} is increased from 1 to 10000 here. From Table VI we can see that the effects of W_{cell} is more obvious for smaller process numbers (e.g., 24 or 48 processes). For larger process numbers, W_{cell} has a slight effects (no more than 10%) on the overall performance. Generally when W_{cell} is too small, the grid re-decomposition will mainly be based on the particle numbers in cells; when W_{cell} is too large, the impact of particles will be ignored, which can also lead to load imbalance. To achieve better performance, users need to specify an appropriate W_{cell} according to their specific simulation configurations.

Fig. 13 shows the effects of $Threshold$. Similar to the effect of T , when $Threshold$ is small, the iterations required to meet $l_{ii} > Threshold$ will be less; when $Threshold$ is large, the iterations required to meet $l_{ii} > Threshold$ will be more. As we can see from Fig. 13, smaller $Threshold$ is slightly better than big $Threshold$ when using no more than 96 processes.

TABLE VI
THE TOTAL EXECUTION TIME IN SECONDS UNDER DIFFERENT W_{cell} FOR THE DC STRATEGY ON TIANHE-2

	Number of Processes						
	24	48	96	192	384	768	1536
$W_{cell} = 1$	2258	1230	706	445	317	240	245
$W_{cell} = 10$	2288	1255	705	437	301	234	239
$W_{cell} = 100$	2258	1240	689	420	292	228	232
$W_{cell} = 1000$	2231	1184	668	408	285	225	228
$W_{cell} = 10000$	2623	1420	771	466	316	243	234

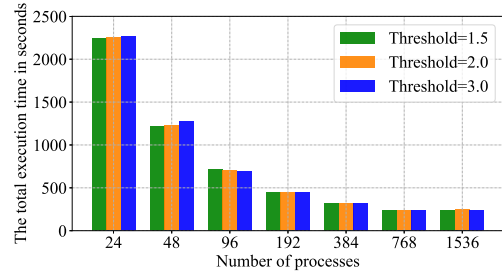


Fig. 13. Effects of $Threshold$ for the DC strategy on Tianhe-2.

The reason is that the load imbalance is more severe when the number of processes is smaller. With the process number increases, $Threshold$ has little effect on the results.

2) *MPI rank placement*: Most of our experiments were conducted on the Tianhe-2 supercomputer. As described in Section VI, this system implements a fat-tree communication topology [32]. This is done by packing 32 computing nodes in a frame where a computing rack has 4 frames. This organization permits three different MPI rank placements: inner-frame, inner-rack and inter-rack. To understand the impact of MPI rank placement, we evaluated our approach under these three MPI placement strategies, using up to 96 processes (16 compute nodes) on *Dataset 2*.

As shown in Fig. 14, different MPI rank placements can have an impact on the performance of the solver. The inner-frame placement outperforms the others because the communication distance between the compute nodes in this placement is smaller than the others. However, the difference is small, around 1% to 2%, indicating the robustness of our approach.

3) *Hardware portability*: We now evaluate the performance of our solver on systems with different hardware architectures and different datasets. In this evaluation, we use four datasets: *Dataset 2*, 4, 5 and 6 in Table I. We test our approach on the x86-based Tianhe-2 supercomputer and the ARMv8-based Tianhe-3 prototype. Among our test datasets, *Dataset 5* and 6 have a large size of grids, and *Dataset 2* and 5 have a large amount of simulation particles.

Fig. 15 shows the performance results on the two computing systems. Our approach exhibits similar strong scalability results on both architectures, indicating the performance portability of our approach. In addition, when using *Dataset 5* and 6 (larger grids), the performance difference between the centralized and the distributed communication strategies

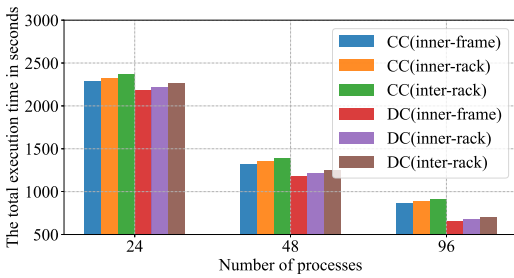


Fig. 14. Impacts of different MPI rank placements for both the CC and DC strategies with dynamic load balance on Tianhe-2.

(Fig. 15(b) and Fig. 15(d)) is smaller than that on *Dataset 2* and *4* (Fig. 15(a) and Fig. 15(c)). Once again, the results suggest that the centralized communication can outperform the distributed communication in certain simulation setups.

VIII. CONCLUSION

We have presented a new approach to optimize large-scale coupled DSMC/PIC particle simulation, using the plasma plume simulation as a case study. We empirically show that centralized and distributed communications can be helpful in particle simulations; each has its advantages in specific simulation setups. Our work addresses a particular challenge in coupled PIC/DSMC simulations – particles can move across grids, leading to load imbalance during dynamic simulation runs. To this end, we design a runtime load balancer to dynamically adjust the work distribution across parallel simulation processes to rebalance the load. We evaluate our parallel-coupled DSMC/PIC solver by applying it to simulate 3D unsteady plasma plume induced by a pulsed vacuum arc. We test the performance of our solver on three distinct HPC platforms. The extensive evaluation shows that our coupled DSMC/PIC solver delivers performance and scaling efficiency, scaling well to thousands of processes with billions of particles.

REFERENCES

- [1] B. D. Smith, I. D. Boyd, H. Kamhawi, and W. Huang, “Hybrid-pic modeling of a high-voltage, high-specific-impulse hall thruster,” 2013.
- [2] B. Korkut, Z. Li, and D. A. Levin, “3-d simulation of ion thruster plumes using octree adaptive mesh refinement,” *IEEE Transactions on Plasma Science*, vol. 43, no. 5, pp. 1706–1721, 2015.
- [3] L. Brieda, S. Z. Tai, and M. Keidar, “Near plume modeling of a micro cathode arc thruster,” in *Aiaa/asm/sae/asee Joint Propulsion Conference*, 2013.
- [4] M. Mozetic, K. Ostrikov, D. N. Ruzic, D. Curreli, U. Cvelbar, A. Vesel, G. Primc, M. Leisch, K. Jousten, and O. B. a. Malyshev, “Recent advances in vacuum sciences and applications,” *Journal of Physics D Applied Physics*, vol. 47, no. 15, p. 153001, 2014.
- [5] Kato, Takahisa, Choi, Junho, Hirata, and Yuki, “Dlc coating on a trench-shaped target by bipolar pbbi,” *International Journal of Refractory Metals & Hard Materials*, 2015.
- [6] F. Taccogna, P. Minelli, D. Bruno, S. Longo, and R. Schneider, “Kinetic divertor modeling,” *Chemical Physics*, vol. 398, no. none, pp. 27–32, 2012.
- [7] C. Gleason-Gonzalez, S. Varoutis, V. Hauer, and C. Day, “Simulation of neutral gas flow in a tokamak divertor using the direct simulation monte carlo method,” *Fusion Engineering & Design*, vol. 89, no. 7–8, pp. 1042–1047, 2014.
- [8] B. G. A., “Direct simulation of the boltzmann equation,” *Physics of Fluids*, vol. 13, no. none, pp. 2676–2681, 1970.

- [9] G. A. Bird, *Molecular gas dynamics*. Molecular Gas Dynamics, Oxford, 1976.
- [10] C. K. Birdsall and A. B. Langdon, *Plasma Physics Via Computer Simulation*. Plasma Physics Via Computer Simulation, 1985.
- [11] R. W. Hockney and J. W. Eastwood, “Computer simulation using particles,” *Institute of Physics*, vol. 76, 1988.
- [12] H. Yaw, “The hungarian method for the assignment problem,” in *Naval Res Logist Quart*, 1955.
- [13] J. Munkres, “Algorithms for the assignment and transportation problems,” *SIAM. J.*, vol. 10, 1962.
- [14] Hopkins, M. Matthew, Boerner, J. Jeremiah, Moore, C. Hudson, Crozier, and P. Stewart, “Addressing challenges to simulating breakdown and arc evolution in vacuum and low pressure systems.” 2013.
- [15] M. M. Hopkins, J. J. Boerner, C. H. Moore, P. S. Crozier, and M. T. Bettencourt, “Ppps-2013: Accommodating large temporal, spatial, and particle weighting demands for simulating vacuum arc discharge,” in *Abstracts IEEE International Conference on Plasma Science*, 2013.
- [16] M. M. Hopkins, R. P. Manginell, J. J. Boerner, C. H. Moore, and M. W. Moorman, “Fully kinetic simulation of atmospheric pressure microcavity discharge device,” in *IEEE International Conference on Plasma Sciences*, 2015, pp. 1–1.
- [17] P. Ortwein, T. Binder, S. Copplestone, A. Mirza, and C. D. Munz, “Parallel performance of a discontinuous galerkin spectral element method based pic-dsmc solver,” 2015.
- [18] S. Copplestone, P. Ortwein, C. D. Munz, T. Binder, and S. Fasoulas, “Coupled pic-dsmc simulations of a laser-driven plasma expansion,” *Springer International Publishing*, 2016.
- [19] C., Johnson, J., and Pitkgranta, “An analysis of the discontinuous galerkin method for a scalar hyperbolic equation,” *Math. Comp.*, 1986.
- [20] B. Korkut and D. A. Levin, “Three dimensional dsmc-pic simulations of ion thruster plumes with sugar,” in *Aiaa/asm/sae/asee Joint Propulsion Conference*, 2014.
- [21] J. Revathi and D. A. Levin, “Chaos: An octree-based pic-dsmc code for modeling of electron kinetic properties in a plasma plume using mpi-cuda parallelization,” *Journal of Computational Physics*, vol. 373, pp. 571–604, 2018.
- [22] J. Li, D. Ingham, L. Ma, N. Wang, and M. Pourkashanian, “Numerical simulation of the chemical combination and dissociation reactions of neutral particles in a rarefied plasma arc jet,” *IEEE Transactions on Plasma Science*, vol. 45, no. 3, pp. 461–471, 2017.
- [23] Y. Su, J. Li, H. Wang, and A. Xu, “Numerical simulation of chemical reactions on rarefied plasma plume by dsmc method,” *IEEE Transactions on Plasma Science*, vol. PP, no. 99, pp. 1–13, 2021.
- [24] G. A. Bird, “Definition of mean free path for real gases,” *Physics of Fluids*, vol. 26, no. 11, pp. 3222–3223, 1983.
- [25] J. P. Boris, “Relativistic plasma simulations – optimization of a hybrid code,” 1970.
- [26] E. Lima, F. W. Tavares, and E. B. Jr, “Finite volume solution of the modified poisson-boltzmann equation for two colloidal particles,” *Physical Chemistry Chemical Physics*, vol. 9, no. 24, pp. 3174–3180, 2007.
- [27] K. L. U. of Minnesota. (2013) Metis - serial graph partitioning and fill-reducing matrix ordering. [Online]. Available: <http://glaros.dtc.umn.edu/gkhome/metis/metis/overview>
- [28] Y. H. Tseng and J. H. Ferziger, “A ghost-cell immersed boundary method for flow in complex geometry,” *Journal of Computational Physics*, vol. 192, no. 2, pp. 593–623, 2003.
- [29] J. Liesen and Z. Strakos, *Krylov subspace methods: principles and analysis*. Oxford University Press, 2013.
- [30] A. N. Laboratory. (2021) Petsc 3.16 — petsc 3.16.0 documentation. [Online]. Available: <https://petsc.org/release/>
- [31] Z. Wang and M. O’Boyle, “Machine learning in compiler optimization,” *Proceedings of the IEEE*, vol. 106, no. 11, pp. 1879–1901, 2018.
- [32] X. Liao, L. Xiao, C. Yang, and L. U. Yutong, “Milkyway-2 supercomputer: system and application,” *Frontiers of Computer Science*, vol. 8, no. 3, 2014.
- [33] Y. S. Li, X. H. Chen, J. Liu, B. Yang, and H. Xu, “Ohtma: an optimized heuristic topology-aware mapping algorithm on the tianhe-3 exascale supercomputer prototype,” *Frontiers of Information Technology & Electronic Engineering*, vol. 21, no. 6, pp. 939–949, 2020.
- [34] O. CASCADE. Salome - the open source integration platform for numerical simulation. [Online]. Available: <https://www.salome-platform.org/>

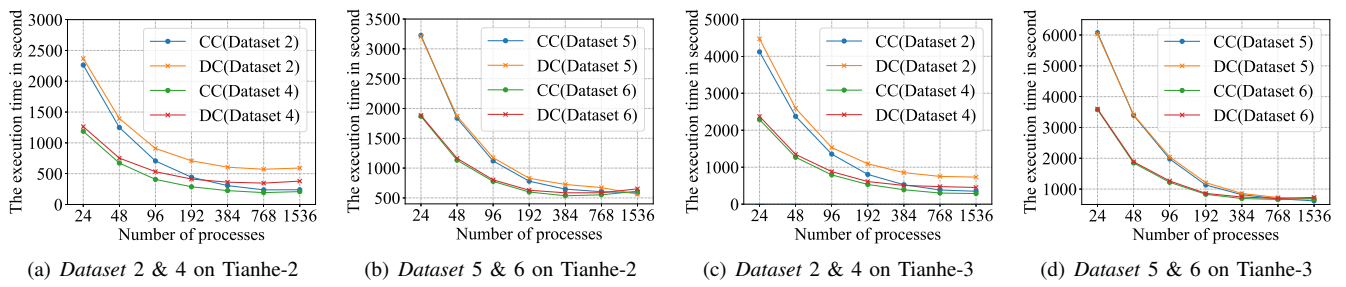


Fig. 15. Performance of the two communication strategies with dynamic load balance on Tianhe-2 ((a) and (b)) and the Tianhe-3 prototype ((c) and (d)).